

# CM-NAS: Rethinking Cross-Modality Neural Architectures for Visible-Infrared Person Re-Identification

Chaoyou Fu<sup>1,2\*</sup> Yibo Hu<sup>3\*</sup> Xiang Wu<sup>1</sup> Hailin Shi<sup>3</sup> Tao Mei<sup>3</sup> Ran He<sup>1,2†</sup>

<sup>1</sup> NLPR & CEBSIT & CRIPAC, CASIA

<sup>2</sup> University of Chinese Academy of Sciences

<sup>3</sup> JD AI Research

{chaoyou.fu, rhe}@nlpr.ia.ac.cn, {shihailin, tmei}@jd.com

{huyibo871079699, alfredxiangwu}@gmail.com

## Abstract

*Visible-Infrared person re-identification (VI-ReID) aims at matching cross-modality pedestrian images, breaking through the limitation of single-modality person ReID in dark environment. In order to mitigate the impact of large modality discrepancy, existing works manually design various two-stream architectures to separately learn modality-specific and modality-sharable representations. Such a manual design routine, however, highly depends on massive experiments and empirical practice, which is time consuming and labor intensive. In this paper, we systematically study the manually designed architectures, and identify that appropriately splitting Batch Normalization (BN) layers to learn modality-specific representations will bring a great boost towards cross-modality matching. Based on this observation, the essential objective is to find the optimal splitting scheme for each BN layer. To this end, we propose a novel method, named Cross-Modality Neural Architecture Search (CM-NAS). It consists of a BN-oriented search space in which the standard optimization can be fulfilled subject to the cross-modality task. Besides, in order to better guide the search process, we further formulate a new Correlation Consistency based Class-specific Maximum Mean Discrepancy ( $C^3MMD$ ) loss. Apart from the modality discrepancy, it also concerns the similarity correlations, which have been overlooked before, in the two modalities. Resorting to these advantages, our method outperforms state-of-the-art counterparts in extensive experiments, improving the Rank-1/mAP by **6.70%/6.13%** on SYSU-MM01 and **12.17%/11.23%** on RegDB. The source code will be released soon.*

## 1. Introduction

Person re-identification (ReID) refers to matching pedestrian images acquired from disjoint cameras [21, 59, 67]. In recent years, it has received substantial attention due to its significant practical value in video surveillance [52]. Conventional person ReID is only devoted to single-modality, *i.e.* all the person images are taken by visible cameras during day time. Benefiting from the strenuous efforts of researchers, impressive achievements have been made on most benchmarks [62, 1, 58, 60]. Nevertheless, the visible cameras cannot image clearly in dark environment, which impedes the popularization and application of person ReID [42]. To overcome this obstacle, in addition to the visible (VIS) cameras, infrared (IR) cameras that are robust to illumination variants are also equipped in many surveillance scenarios [5]. Therefore, in practice, we often need to match VIS and IR pedestrian images, raising the task of VI-ReID.

Modality discrepancy, caused by different wavelengths of VIS and IR images, is one of the most difficult challenges in VI-ReID. Existing works have manually designed various two-stream architectures [54, 55, 27] to mitigate the impact of the large modality discrepancy. Specifically, some layers are split into two branches to learn modality-specific representations for VIS and IR data respectively, while the remaining layers are shared to learn modality-sharable representations. The intuition behind this design is that VIS and IR images contain both modality-specific information, *e.g.* the spectrum, and modality-sharable information, *e.g.* the identity. At this point, an obvious problem is raised: which layers should be split into two branches and which layers should be shared? Some methods split the layers in the first one [52, 55] or five [57] blocks, while some others share the whole network [46]. There is still no consensus on the optimal design of the neural architecture for VI-ReID.

In this paper, by investigating the impact of splitting different layers, we rethink the manually designed neural

\*Equal contribution. This work was done during an internship of Chaoyou Fu at JD AI Research.

†Corresponding author.

architectures for VI-ReID. As illustrated in Section 3.1, our empirical study suggests that **appropriately splitting Batch Normalization (BN) layers will bring a great boost towards cross-modality matching**. Based on this observation, the essential objective is to find the optimal splitting scheme for each BN layer in the backbone. However, there are a great deal of potential splitting schemes. Specifically, the backbone ResNet50 [15] contains 49 BN layers, leading to a total of  $2^{49}$  possible architectures. It is time consuming and labor intensive to manually traverse through all the possible architectures. In order to tackle this intractable problem, benefiting from the recently thriving Neural Architecture Search (NAS) [28, 18, 38, 6], we propose a novel Cross-Modality NAS (CM-NAS) to automatically determine whether each BN layer splits or not. A BN-oriented search space is elaborately built in which the standard optimization can be fulfilled subject to the cross-modality task. As far as we know, this is the first NAS-based method developed specially for cross-modality person ReID. Besides, in order to better guide the search process, we further formulate a Correlation Consistency based Class-specific Maximum Mean Discrepancy ( $C^3$ MMD) loss. In addition to the modality discrepancy, it also pays attention to the similarity correlations, which have been ignored before, among features in the two modalities.

To sum up, we make the following four contributions:

- We analyze the manually designed neural architectures in detail, and identify the significance of appropriately splitting the BN layers. This observation motivates us to develop a BN-oriented search algorithm.
- A novel CM-NAS is proposed to automatically search the optimal architecture for VI-ReID. To the best of our knowledge, this is the first NAS-based method for the cross-modality person ReID.
- A new  $C^3$ MMD loss is introduced to guide the search process. Besides the modality discrepancy,  $C^3$ MMD also focuses on the similarity correlations that have been neglected before in the two modalities.
- Our method surpasses state-of-the-art methods by a large margin, improving the Rank-1/mAP by **6.70%/6.13%** on the SYSU-MM01 dataset and **12.17%/11.23%** on the RegDB dataset.

## 2. Related Works

**Single-Modality Person ReID.** The goal of single-modality person ReID is to match pedestrian VIS images across non-overlapping visible cameras [12, 64]. Existing works can be divided into three categories, including hand-crafted descriptors methods [32, 51, 25, 63], metric learning methods [65, 26] and the deep learning methods

[17, 37, 31, 66, 23, 44, 41, 16]. The hand-crafted descriptors methods are dedicated to manually designing effective features [51]. The metric learning methods aim at minimizing the distance between a positive pair and maximizing that between a negative pair [20]. The deep learning methods employ deep neural networks to directly learn features [24, 7]. However, the visible cameras cannot image clearly in dark environment, which impedes the popularization and application of the single-modality person ReID [61, 42].

**Visible-Infrared Person ReID.** Different from the aforementioned single-modality person ReID, VI-ReID matches pedestrian images belonging to different modalities. Due to the great practical value of VI-ReID, it has received substantial attention in recent years [10, 42, 30, 55]. The pioneer work [46] contributes a new VI-ReID dataset named SYSU-MM01 and introduces a deep zero-padding method, which explores modality-specific information in a one-stream network. [5] proposes a cross-modality generative adversarial framework to reduce the modality discrepancy. [14] employs a two-stream HSMEnet to map both representation learning and metric learning on to a hypersphere manifold. Benefiting from the paired image generation, [43] has the ability to simultaneously align set-level and instance-level cross-modality features.

**Neural Architecture Search.** Existing NAS works can be grouped into micro search methods and macro search methods [18]. The micro search methods aim at designing robust cells and then stacking these cells to constitute the neural architecture. Traditional methods mainly depend on evolutionary algorithms or reinforcement learning to tackle the discrete search problem [36, 68]. Recently, DARTS [28] first proposes a differentiable search strategy, which greatly reduces the computational overhead compared with the traditional methods [8, 49, 4]. The macro search methods search the whole neural architecture, which is thought to be more flexible than searching cells [3, 39]. [2] introduces Q-learning to select layers sequentially. [47] searches accurate and efficient architectures for mobile devices. However, these methods are all designed for single-modality tasks, with no need for considering the modality discrepancy.

## 3. Method

### 3.1. Rethinking Manually Designed Architectures

For fair comparisons with other VI-ReID methods, we employ ResNet50<sup>1</sup> pre-trained on ImageNet as the backbone, whose architecture is reported in Table 1. There are 5 stages in ResNet50, where each stage consists of blocks,

<sup>1</sup>Other networks are also applicable.

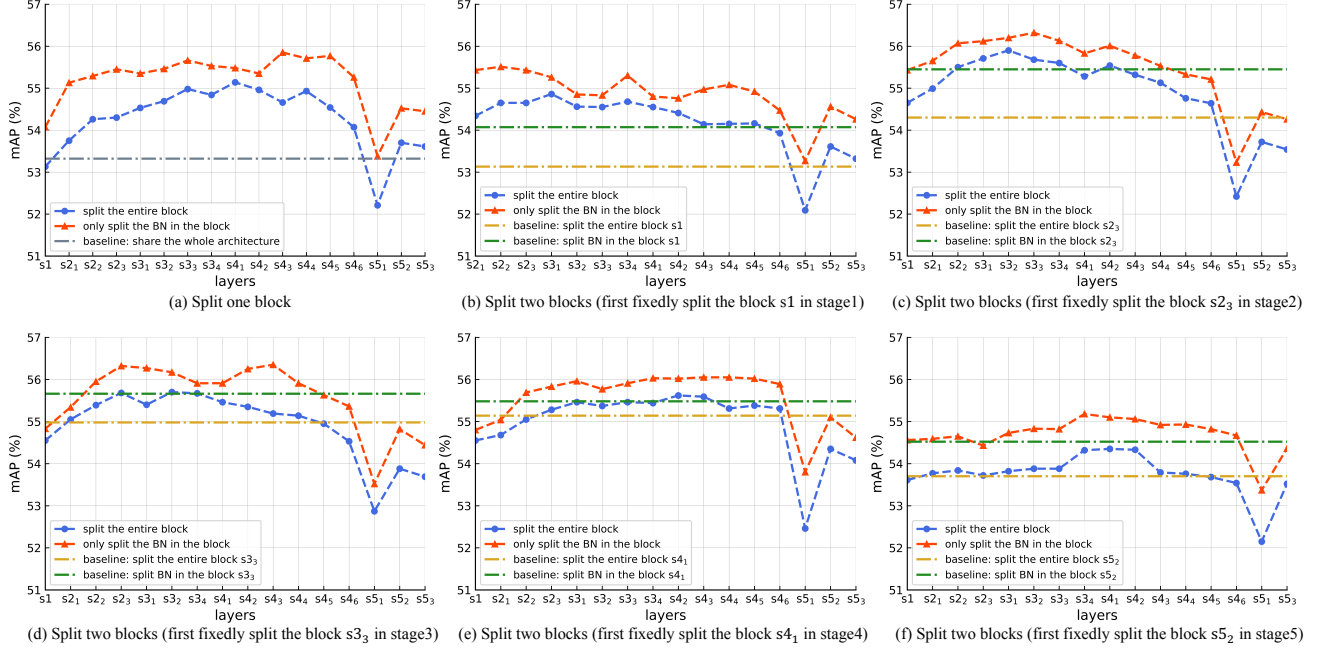


Figure 1. Comparisons of different ResNet50-based architecture designs on the SYSU-MM01 dataset under the challenging *single-shot&all-search* setting [46]. ‘s<sub>21</sub>’ denotes the 1-th block in stage2 of ResNet50, whose architecture is listed in Table 1. We design the architecture in units of the entire block (the blue line) or only the BN layers in the block (the red line). (a) shows the results of merely splitting one block. (b)-(f) present the results of splitting two blocks, where we first fixedly split a block and then traverse through the remaining stages to split the other one. Note that for (c), we choose to first fixedly split the block ‘s<sub>23</sub>’ rather than ‘s<sub>21</sub>’ or ‘s<sub>22</sub>’ in stage2, because ‘s<sub>23</sub>’ performs better than the others in (a). (d)-(f) are also in the same way. It is obvious that splitting two blocks generally achieves better results than splitting a single one, especially when only splitting the BN layers in the block.

Table 1. The architecture of ResNet50 [15] that includes 5 stages. ‘s<sub>2x</sub>’ denotes the x-th ResBlock in stage2. A ConvBlock has one convolution layer, one BN layer [19] and one ReLU layer. A ResBlock contains a total of three convolution layers, three BN layers and three ReLU layers. Please refer to [15] for details.

| Name   | s1          | s2 <sub>x</sub> | s3 <sub>x</sub> | s4 <sub>x</sub> | s5 <sub>x</sub> |
|--------|-------------|-----------------|-----------------|-----------------|-----------------|
| Layers | 1 ConvBlock | 3 ResBlocks     | 4 ResBlocks     | 6 ResBlocks     | 3 ResBlocks     |

including ConvBlock and ResBlock. As mentioned in Section 1, due to the absence of consensus on the optimal splitting scheme for the neural architecture, we conduct systematic experiments to assess the impact of different architecture designs. In general, the architecture is designed in units of the entire block [54, 55], such as splitting one or five blocks into two branches [57, 27]. Besides, we also design the architecture in units of the BN layers in the block, *i.e.* only splitting the BN layers rather than all the layers in the block. This is motivated by a recent study [48], which reveals that separating BN layers for the data from different domains performs better than sharing BN layers.

First of all, we evaluate the performance of splitting one block (splitting all the layers in the block or only the BN layers in the block). Concretely, we split the blocks in ResNet50 one by one to learn modality-specific representations, and share the remaining to learn modality-sharable

representations. Fig. 1 (a) depicts the results of all the potential architectures as well as the result of one baseline model: sharing the whole architecture without splitting. We have three major observations from Fig. 1 (a): (1) the baseline generally performs worse than splitting one block, suggesting the necessity of splitting blocks to learn modality-specific representations; (2) splitting different blocks yields much different performances. For example, when splitting the entire block, ‘s<sub>41</sub>’ and ‘s<sub>51</sub>’ lead to the best and the worst results, respectively. It implies that we need to carefully treat each layer in the design process; (3) splitting the BN layers in the block is more suitable than splitting the entire block, since the former (the red line) gains much better results than the latter (the blue line) in all splitting schemes. Subsequently, we further split two blocks for each time. Fig. 1 (b)-(f) display the results when we first fixedly split a block in stage1, stage2, stage3, stage4 and stage5 respectively, and then traverse through the remaining stages to split the other one. The performance of splitting one block in the first step is also reported as a baseline result. A *major observation from these results is that splitting two blocks generally achieves better results than splitting a single one, especially when only splitting the BN layers in the block.*

With these observations, we arrive at a conclusion that

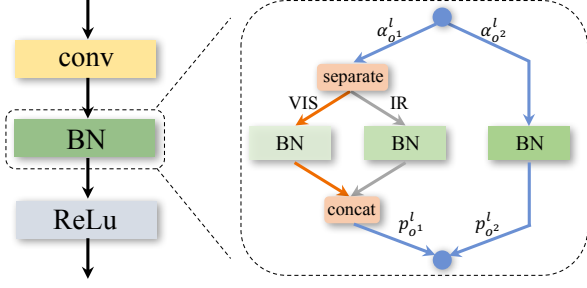


Figure 2. The BN-oriented search space of CM-NAS. All BN layers in the backbone are reshaped as searchable units. Each BN layer has two candidate operations: employing two separate parameters for VIS and IR data respectively, or sharing its parameters for the data of both two modalities.

appropriately splitting more BN layers can lead to better performances. Hence, the essential objective is to find the optimal splitting scheme for each BN layer in the backbone. As illustrated in Section 1, since it is intractable to manually traverse through all potential architectures, we introduce a novel NAS algorithm to automatically search the best one.

### 3.2. Cross-Modality NAS

Inspired by the above analyses, our architecture design revolves around which BN layers should be split and which BN layers should be shared. In light of this, we design a BN-oriented search space that is depicted in Fig. 2. In our search space, all BN layers in the backbone are reshaped as searchable units and each BN layer has two candidate operations: employing separate or shared parameters. If a BN layer chooses the former, this BN layer will have two separate parameters that are learned from VIS and IR data, respectively. Otherwise, this BN layer will share parameters that are learned from the data of both two modalities.

Formally, let  $o^1$  and  $o^2$  denote the above two candidate operations, respectively. In each BN layer  $l$ , we assign an architecture parameter  $\alpha_{o^1}^l$  to the operation  $o^1$  and the other architecture parameter  $\alpha_{o^2}^l$  to the remaining operation  $o^2$ . When  $\alpha_{o^1}^l = 1$  and  $\alpha_{o^2}^l = 0$ , it means that the BN layer  $l$  adopts two separate parameters. Otherwise, when  $\alpha_{o^1}^l = 0$  and  $\alpha_{o^2}^l = 1$ , the BN layer  $l$  shares its parameters. In practice, instead of searching on such discrete candidate architectures, we relax the search space to make it can be optimized via gradient descent [28]. Concretely, we relax the binary architecture parameter  $\alpha_{o^i}^l$  ( $i \in \{1, 2\}$ ) to be continuous, and then obtain the probability of choosing the corresponding operation by computing a softmax over all architecture parameters:

$$p_{o^i}^l = \frac{\exp(\alpha_{o^i}^l)}{\exp(\alpha_{o^1}^l) + \exp(\alpha_{o^2}^l)}. \quad (1)$$

The larger the value of  $p_{o^i}^l$ , the more likely the BN layer  $l$  is to choose the operation  $o^i$ . The output of the BN layer  $l$  is

a weighted sum of all possible operations:

$$x_{l+1} = p_{o^1}^l \cdot o_1(x_l) + p_{o^2}^l \cdot o_2(x_l), \quad (2)$$

where  $o_i(x_l)$  denotes that the operation  $o_i$  is applied to the input  $x_l$ . In such a case, the search process is transformed into the learning of a set of architecture parameters  $\alpha = \{\alpha_{o^i}^l\}$ . Furthermore, since the network weights  $w$ , such as the weights of convolution layers, also need to be learned, we are required to tackle the following bi-level optimization problem [28, 8, 47]:

$$\begin{aligned} \min_{\alpha} \mathcal{L}_{\text{val}}(w^*, \alpha). \\ \text{s.t. } w^* = \arg \min_w \mathcal{L}_{\text{train}}(w, \alpha) \end{aligned} \quad (3)$$

The goal of Eq. (3) is to search architecture parameters  $\alpha^*$  that minimize the validation loss  $\mathcal{L}_{\text{val}}(w^*, \alpha^*)$ , where the network weights  $w^*$  are obtained by minimizing the training loss  $\mathcal{L}_{\text{train}}(w, \alpha)$ . After training, for each BN layer  $l$ , we choose the operation with a larger probability and abandon the other one, yielding a discrete architecture. For instance, when  $p_{o^1}^l > p_{o^2}^l$ , we will choose the operation  $o_1$ , i.e. employing two separate parameters in the BN layer  $l$ . In addition, it is obvious that the training and the validation losses play critical roles in the search process, which are introduced in the following subsection.

### 3.3. C<sup>3</sup>MMD

The cross-modality property makes VI-ReID more challenging than the traditional single-modality person ReID [42]. This is because the large modality discrepancy results in a large intra-class distance that degrades the accuracy of feature matching. How to reduce the modality discrepancy to learn modality invariant features has always been a hot research topic [11].

For such a cross-modality problem involved in VI-ReID, Maximum Mean Discrepancy (MMD) [13] is an effective metric to measure the modality discrepancy. MMD compares two distributions  $p_{\text{vis}}$  and  $p_{\text{ir}}$  via a test statistic, aiming at finding a smooth function that maximizes the mean discrepancy between the two distributions. Let  $f^{\text{vis}} = \Phi(x^{\text{vis}}, w)$  and  $f^{\text{ir}} = \Phi(x^{\text{ir}}, w)$  be the VIS and the IR embedding features sampled from  $p_{\text{vis}}$  and  $p_{\text{ir}}$ , respectively.  $\Phi(\cdot | \alpha, w)$  denotes the output of the searchable supernet defined in Section 3.2. A function  $\psi(\cdot)$  is further introduced to map these features into a universal Reproducing Kernel Hilbert Space (RKHS), in which the MMD can be formulated as:

$$\text{MMD} = \sup_{\|\psi\|_{\mathcal{H}} \leq 1} \left| \mathbb{E}_{f^{\text{vis}}} [\psi(f^{\text{vis}})] - \mathbb{E}_{f^{\text{ir}}} [\psi(f^{\text{ir}})] \right|_{\mathcal{H}}, \quad (4)$$

where  $\|\psi\|_{\mathcal{H}} \leq 1$  means that the set of functions in a unit ball of the RKHS. Moreover, when  $\psi$  is represented by a

kernel  $k(f^{vis}, f^{ir})$ , the empirical estimation of MMD is defined as:

$$\text{MMD} = \left\| \frac{1}{m} \sum_{i=1}^m \psi(f_i^{vis}) - \frac{1}{n} \sum_{j=1}^n \psi(f_j^{ir}) \right\|_{\mathcal{H}}, \quad (5)$$

where  $m$  and  $n$  are the number of the features  $f^{vis}$  and  $f^{ir}$ , respectively. It is obvious that minimizing Eq. (5) will bridge the distribution gap between  $p_{vis}$  and  $p_{ir}$  [34, 29, 50], *i.e.* reducing the modality discrepancy between the VIS and the IR features. Considering that there are class labels in our VI-ReID task, we establish the MMD loss for each class separately to reduce the intra-class distance. Suppose there are a total of  $C$  classes, the class-specific MMD loss is formulated as:

$$\mathcal{L}_{\text{CMMD}} = \frac{1}{C} \sum_{c=1}^C \left\| \frac{1}{m^c} \sum_{i=1}^{m^c} \psi(f_i^{c,vis}) - \frac{1}{n^c} \sum_{j=1}^{n^c} \psi(f_j^{c,ir}) \right\|_{\mathcal{H}}, \quad (6)$$

where  $m^c$  and  $n^c$  denote the number of the VIS and the IR data belonging to the  $c$ -th class, respectively.

Furthermore, we observe that the performance of the above  $\mathcal{L}_{\text{CMMD}}$  is unsatisfactory in the experiment, which is discussed in Section 4.2. We argue that this is because the MMD loss merely concerns the overall modality discrepancy, while ignores the similarity correlations among features in the two modalities. Specifically, since the similarity correlation should also be modality irrelevant, we need to keep the consistency of the similarity correlations in the two modalities during reducing modality discrepancy, as shown in Fig. 3. Such correlation consistency has been fully explored in recently proposed knowledge distillation works [35, 40], but has never been studied in VI-ReID. Moreover, unlike [35, 40] that concern the correlations in the student and the teacher networks, we focus on the correlations of different modality data in one network.

Formally, let  $\mathbf{F}_{vis}$  and  $\mathbf{F}_{ir}$  be the set of embedding features of the VIS and the IR data respectively:

$$\begin{aligned} \mathbf{F}_{vis} &= \text{matrix}(f_1^{vis}, f_2^{vis}, \dots, f_n^{vis}), \\ \mathbf{F}_{ir} &= \text{matrix}(f_1^{ir}, f_2^{ir}, \dots, f_n^{ir}). \end{aligned} \quad (7)$$

In practice, we sample  $n$  VIS and  $n$  IR images for each time, because constraining the correlation consistency requires the same number of data [40]. Meanwhile,  $f_i^{vis}$  and  $f_i^{ir}$  ( $i \in \{1, \dots, n\}$ ) belong to the same identity. Inspired by [40], the correlation matrices  $\tilde{\mathbf{G}}_{vis}$  and  $\tilde{\mathbf{G}}_{ir}$  that reflect the pairwise similarities among features in the embedding space can be computed as:

$$\tilde{\mathbf{G}}_{vis} = \mathbf{F}_{vis} \cdot \mathbf{F}_{vis}^\top, \quad \tilde{\mathbf{G}}_{ir} = \mathbf{F}_{ir} \cdot \mathbf{F}_{ir}^\top. \quad (8)$$

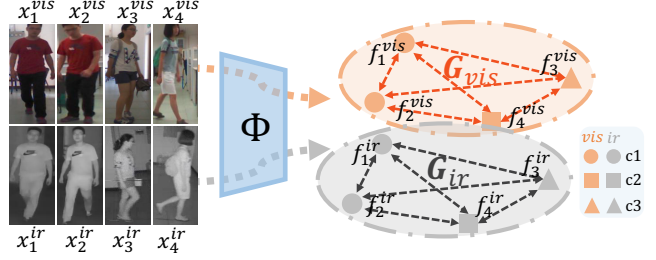


Figure 3. The illustration of the correlation consistency loss  $\mathcal{L}_{\text{CC}}$  in  $\text{C}^3\text{MMD}$ .  $\Phi$  is the searchable supernet.  $f_i^{vis}$  and  $f_i^{ir}$  are the features of the VIS image  $x_i^{vis}$  and the IR image  $x_i^{ir}$ , respectively.  $x_i^{vis}$  and  $x_i^{ir}$  belong to the same class.  $\mathbf{G}_{vis}$  and  $\mathbf{G}_{ir}$  denote the similarity correlations, which have been neglected before, among the features in the VIS and the IR modalities, respectively.  $\mathcal{L}_{\text{CC}}$  encourages the consistency between  $\mathbf{G}_{vis}$  and  $\mathbf{G}_{ir}$ .

Then, a row-wise  $L_2$  normalization is applied on the two correlation matrices:

$$\mathbf{G}_{vis[i,:]} = \frac{\tilde{\mathbf{G}}_{vis[i,:]}^T}{\|\tilde{\mathbf{G}}_{vis[i,:]}^T\|_2}, \quad \mathbf{G}_{ir[i,:]} = \frac{\tilde{\mathbf{G}}_{ir[i,:]}^T}{\|\tilde{\mathbf{G}}_{ir[i,:]}^T\|_2}, \quad (9)$$

where the notation  $[i,:]$  denotes the  $i$ -th row in a matrix. A correlation consistency loss  $\mathcal{L}_{\text{CC}}$  is further developed to penalize the difference between  $\mathbf{G}_{vis}$  and  $\mathbf{G}_{ir}$ :

$$\mathcal{L}_{\text{CC}} = \frac{1}{n^2} \|\mathbf{G}_{vis} - \mathbf{G}_{ir}\|_F^2, \quad (10)$$

where  $\|\cdot\|_F$  denotes a Frobenius norm. Our  $\text{C}^3\text{MMD}$  loss is a weighted sum of the class-specific MMD loss and the correlation consistency loss:

$$\mathcal{L}_{\text{C}^3\text{MMD}} = \lambda_1 \mathcal{L}_{\text{CMMD}} + \lambda_2 \mathcal{L}_{\text{CC}}, \quad (11)$$

where  $\lambda_1$  and  $\lambda_2$  are trade-off parameters.

In addition to the above  $\mathcal{L}_{\text{C}^3\text{MMD}}$ , our objective function also includes a basic loss  $\mathcal{L}_{\text{basic}}$  [43, 55] that consists of a classification loss  $\mathcal{L}_{\text{cls}}$  and a triplet loss  $\mathcal{L}_{\text{triplet}}$  to learn embedding features. Finally, the training loss  $\mathcal{L}_{\text{train}}$  in Eq. (3) is the combination of the basic loss  $\mathcal{L}_{\text{basic}}$  and the  $\text{C}^3\text{MMD}$  loss  $\mathcal{L}_{\text{C}^3\text{MMD}}$ :

$$\mathcal{L}_{\text{train}} = \mathcal{L}_{\text{basic}} + \mathcal{L}_{\text{C}^3\text{MMD}}. \quad (12)$$

The validation loss  $\mathcal{L}_{\text{val}}$  in Eq. (3) has the same form as the training loss.

## 4. Experiment

### 4.1. Experimental Settings

**Dataset.** SYSU-MM01 [46] is a pioneer benchmark for the research of VI-ReID. This dataset consists of a total of 287,628 VIS images taken by 4 VIS cameras in the day-time, and 15,792 near-IR images taken by 2 near-IR cameras in the dark environment. These images are captured in

both indoor and outdoor scenarios with abundant poses and viewpoints. The training set and the testing set have 395 and 96 person identities, respectively. Following [46], there are two testing models: *all-search* and *indoor-search*. For the former, the gallery set contains VIS images in both indoor and outdoor scenarios. For the latter, the gallery set merely contains VIS images in the indoor scenario. Besides, for both models, there are also two settings: *single-shot* and *multi-shot*. It means 1 or 10 VIS images of a person identity are randomly chosen to be the gallery set.

RegDB [33] is built by a dual camera acquisition system, including a VIS camera and a thermal-IR camera. The two cameras are attached together to take photos at the same time, acquiring a total of 4,120 paired VIS-IR images from 412 person identities (each identity has 10 VIS images and 10 thermal-IR images). Following [53], 2,060 images from 206 person identities are randomly chosen as the training set and the remaining 2,060 images from 206 identities constitute the testing set. There are two evaluation settings: *Visible to Infrared* and *Infrared to Visible*. Take the former for example, it denotes leveraging the VIS images as the probe set and the IR images as the gallery set.

**Evaluation Metrics.** Following existing VI-ReID methods [42, 54, 58], we adopt Cumulative Matching Characteristic (CMC) and mean Average Precision (mAP) as evaluation metrics. Furthermore, the reported result on the SYSU-MM01 dataset is an average performance of 10 times repeated random probe/gallery splits [46], while that on the RegDB dataset is an average performance of 10 times random training/testing splits [53, 45].

**Implementation Details.** We adopt ResNet50 [15] pre-trained on ImageNet as the backbone. The input images are first padded with 10 and then randomly cropped to  $256 \times 128$ . Random horizontal flipping is further imposed as data augmentation. Adam ( $\beta_1=0.5$ ,  $\beta_2=0.999$ ) is employed as the optimizer with  $5e-4$  weight decay. The initial learning rate is set to 0.01 and divided by 10 at the 40-th and the 70-th epochs. The training process is finished at the 120-th epoch. One training batch contains 8 identities and each identity has 4 VIS images as well as 4 IR images. We leverage the polynomial kernel function to calculate the MMD in Eq. (5). The trade-off parameters  $\lambda_1$  and  $\lambda_2$  in Eq. (11) are set to 5.0 and 0.05, respectively. Following the standard process of NAS [28, 9, 18], there are two phases to train the network. In the first phase, all BN layers in the backbone are set to be searchable and Eq. (3) is employed as the loss function, aiming at finding the optimal neural architecture. Since the search needs a validation set, we divide the original training set into a new training set and a validation set by a ratio of identities of 8:2. In the second phase, the architecture of the network is fixed to the best one and we

retrain the network with Eq. (12) for the evaluation of VI-ReID. The training set in the second phase is the original one without splitting the validation set.

## 4.2. Experimental Analyses

**Evaluation of the Search Algorithm.** In this part, we evaluate the effectiveness of the proposed search algorithm in Section 3.2. Concretely, we only employ the basic loss  $\mathcal{L}_{\text{basic}}$  in Eq.(12) as the loss function in both the two phases of NAS. The compared baselines include: (1) a one-stream method that shares the whole architecture for both VIS and IR modalities; (2) a two-stream method that splits the blocks of stage1 and stage2 to learn modality-specific representations, and shares the remaining blocks to learn modality-sharable representations; (3) a BN-oriented two-stream method that only splits BN layers rather than all the layers in blocks of stage1 and stage2. For fair comparisons, these baseline methods are also trained with  $\mathcal{L}_{\text{basic}}$ .

The comparison results on the SYSU-MM01 and the RegDB datasets are reported in the first four rows of Table 2, from which we have three observations. First, the two-stream method achieves better performances than the one-stream method, implying the necessity of splitting blocks. Second, only splitting the BN layers in the block performs better than splitting the entire block, which indicates the significance of the BN layer in learning cross-modality representations. The above two observations are consistent with those in Section 3.1, motivating us to develop a BN-oriented search algorithm to automatically decide the splitting of BN layers. Third, our search algorithm outperforms all the competitors. For instance, the search algorithm exceeds the BN-oriented two-stream method by 2.62% and 1.55% in terms of Rank-1 and mAP on the SYSU-MM01 dataset under the *single-shot&all-search* setting. It demonstrates that our search algorithm can indeed find a more suitable neural architecture for VI-ReID.

**Evaluation of  $\mathcal{C}^3\text{MMD}$ .** In order to verify the effectiveness of  $\mathcal{L}_{\mathcal{C}^3\text{MMD}}$  in Eq. (11), we elaborately design several comparative experiments. Specifically, we add  $\mathcal{L}_{\mathcal{C}^3\text{MMD}}$  to the training of the aforementioned four methods, including the three baselines as well as the search method. Since the search method has two training phases, there are three manners to add  $\mathcal{L}_{\mathcal{C}^3\text{MMD}}$ : (1) only adding  $\mathcal{L}_{\mathcal{C}^3\text{MMD}}$  in the first phase, which means that the first phase is trained with both  $\mathcal{L}_{\text{basic}}$  and  $\mathcal{L}_{\mathcal{C}^3\text{MMD}}$  while the second phase is merely trained with  $\mathcal{L}_{\text{basic}}$ ; (2) only adding  $\mathcal{L}_{\mathcal{C}^3\text{MMD}}$  in the second phase; (3) adding  $\mathcal{L}_{\mathcal{C}^3\text{MMD}}$  in the both two phases. The results of the above methods are listed in the middle six rows of Table 2. For the three baseline methods, compared with the results of only employing  $\mathcal{L}_{\text{basic}}$  (the first four rows), it is obvious that their performances are all improved after adding  $\mathcal{L}_{\mathcal{C}^3\text{MMD}}$ . For example, on the SYSU-MM01 dataset under the *single-*



Table 2. Evaluations of CM-NAS on the SYSU-MM01 dataset under the *all-search* setting as well as the RegDB dataset. R1, R10 and R20 denote Rank-1, Rank-10 and Rank-20 accuracies (%), respectively. mAP denotes the mean average precision score (%). ‘phase1’ and ‘phase2’ are the searching and the training phases of NAS, respectively.

| Method          | $\mathcal{L}_{C^3MMD}$    | SYSU-MM01 (All-Search) |              |              |              |              |              |              |              | RegDB               |              |              |              |                     |              |              |              |
|-----------------|---------------------------|------------------------|--------------|--------------|--------------|--------------|--------------|--------------|--------------|---------------------|--------------|--------------|--------------|---------------------|--------------|--------------|--------------|
|                 |                           | Single-Shot            |              |              |              | Multi-Shot   |              |              |              | Visible to Infrared |              |              |              | Infrared to Visible |              |              |              |
|                 |                           | R1                     | R10          | R20          | mAP          | R1           | R10          | R20          | mAP          | R1                  | R10          | R20          | mAP          | R1                  | R10          | R20          | mAP          |
| one-stream      | $\times$                  | 54.49                  | 89.85        | 95.78        | 53.32        | 61.26        | 85.22        | 92.20        | 46.53        | 75.81               | 90.57        | 95.07        | 71.97        | 74.03               | 90.30        | 94.43        | 70.01        |
| two-stream      | $\times$                  | 56.20                  | 90.62        | 95.83        | 54.22        | 62.70        | 93.44        | 97.61        | 46.87        | 76.93               | 91.24        | 95.39        | 73.02        | 74.51               | 90.46        | 94.66        | 70.55        |
| two-stream (BN) | $\times$                  | 56.94                  | 90.77        | 96.18        | 55.24        | 62.74        | 92.81        | 96.93        | 47.91        | 77.88               | 91.96        | 95.74        | 73.98        | 75.00               | 90.71        | 94.56        | 71.64        |
| search          | $\times$                  | 59.56                  | 91.43        | 96.24        | 56.79        | 66.12        | 94.21        | 97.90        | 49.89        | 78.77               | 92.94        | 96.29        | 76.05        | 77.55               | 92.44        | 95.87        | 74.86        |
| one-stream      | $\checkmark$              | 56.18                  | 90.80        | 96.05        | 54.47        | 63.36        | 93.15        | 97.53        | 47.60        | 77.42               | 91.46        | 95.32        | 74.57        | 75.45               | 90.67        | 94.66        | 71.84        |
| two-stream      | $\checkmark$              | 57.86                  | 90.72        | 96.21        | 55.97        | 64.28        | 93.66        | 97.97        | 48.41        | 78.03               | 91.79        | 95.37        | 74.96        | 75.52               | 90.77        | 94.68        | 72.04        |
| two-stream (BN) | $\checkmark$              | 57.94                  | 91.70        | 96.76        | 56.30        | 65.05        | 93.58        | 97.88        | 49.33        | 78.48               | 92.65        | 96.27        | 75.53        | 75.87               | 91.10        | 94.64        | 73.10        |
| search          | phase1                    | 59.55                  | 91.83        | 96.93        | 57.62        | 66.72        | 94.52        | 97.63        | 50.73        | 79.71               | 93.25        | 96.38        | 76.65        | 78.20               | 92.70        | 96.04        | 75.28        |
| search          | phase2                    | 59.95                  | 91.74        | 96.80        | 57.72        | 66.93        | 94.55        | 97.96        | 51.02        | 82.36               | 94.16        | 97.27        | 78.83        | 81.20               | 93.63        | 96.54        | 77.14        |
| search          | phases1&2                 | <b>61.99</b>           | <b>92.87</b> | <b>97.25</b> | <b>60.02</b> | <b>68.68</b> | <b>94.92</b> | <b>98.36</b> | <b>53.45</b> | <b>84.54</b>        | <b>95.18</b> | <b>97.85</b> | <b>80.32</b> | <b>82.57</b>        | <b>94.51</b> | <b>97.37</b> | <b>78.31</b> |
| search          | w/o $\mathcal{L}_{CMMMD}$ | 60.77                  | 91.73        | 96.46        | 58.74        | 67.56        | 94.69        | 98.14        | 51.93        | 82.18               | 94.41        | 97.69        | 78.92        | 81.53               | 93.98        | 96.86        | 77.45        |
| search          | w/o $\mathcal{L}_{CC}$    | 60.27                  | 91.96        | 96.77        | 58.45        | 67.25        | 94.50        | 98.09        | 51.39        | 83.75               | 94.86        | 97.84        | 79.72        | 81.87               | 94.29        | 97.09        | 77.45        |

*shot&all-search* setting, the Rank-1 accuracy and the mAP score of the BN-oriented two-stream method increase by 1.0% and 1.06%, respectively. Such improvements reveal the effectiveness of the proposed  $C^3MMD$  loss. For the search method, we can see that adding  $\mathcal{L}_{C^3MMD}$  in the both two phases performs better than adding it in only one phase.

Furthermore, we also investigate the effect of the two components in the  $C^3MMD$  loss, *i.e.* the class-specific MMD loss  $\mathcal{L}_{CMMMD}$  and the correlation consistency loss  $\mathcal{L}_{CC}$ . The results of the ablation study of the two losses are shown in the bottom two rows of Table 2. We find that removing any component leads to the degradation of performances, suggesting the essential roles of both  $\mathcal{L}_{CMMMD}$  and  $\mathcal{L}_{CC}$ .

**Parameter Analyses.** We analyze the two trade-off parameters  $\lambda_1$  and  $\lambda_2$  in Eq. (11) on the SYSU-MM01 dataset under the challenging *single-shot&all-search* setting. The results of the Rank-1 and the mAP of CM-NAS with different  $\lambda_1$  and  $\lambda_2$  are exhibited in Fig. 4. We can observe that our method is not sensitive to the parameters  $\lambda_1$  and  $\lambda_2$  in a large range. For instance, when  $\lambda_1$  changes from 0.01 to 0.1, the Rank-1 accuracy merely changes 0.67%. Moreover, the performance drops when the parameters are set too large, such as  $\lambda_1 = 0.2$  or  $\lambda_2 = 15$ . The most suitable parameter setting is that  $\lambda_1 = 0.05$  and  $\lambda_2 = 5.0$ .

#### 4.3. Comparisons with State-of-the-Art Methods

In this subsection, we compare our proposed CM-NAS with current state-of-the-art VI-ReID methods on the SYSU-MM01 and the RegDB datasets. The compared methods include Zero-Pad [46], TONE [53], HCML [53], cmGAN [5], BDTR [54], eBDTR [54], HSME [14], D<sup>2</sup>RL [45], MSR [10], AlignGAN [42], JSIA-ReID [43], Xmodal [22], MACE [52], cm-SSFT [30], DDAG [55] and HAT [56]. Note that the multi-query setting of cm-SSFT employs all gallery samples to constitute an auxiliary set in each feature matching process, which is infeasible in many real scenarios and unfair to other methods. Therefore, we

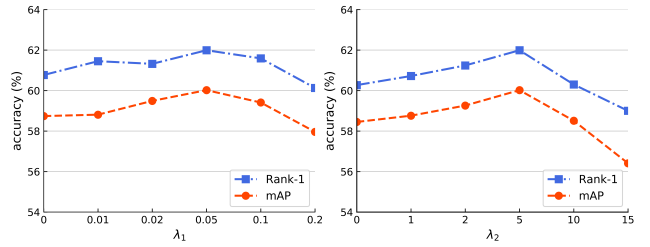


Figure 4. Parameter analyses of  $\lambda_1$  and  $\lambda_2$  in Eq. (11) on the SYSU-MM01 dataset under the *single-shot&all-search* setting. We first fix  $\lambda_2$  to 5.0 and vary the value of  $\lambda_1$  (left). Then, we fix  $\lambda_1$  to 0.05 and vary the value of  $\lambda_2$  (right). The Rank-1 accuracies and mAP scores are reported for comparisons.

only report the results of cm-SSFT under the single-query setting [30] that is consistent with other VI-ReID methods.

**Comparisons on SYSU-MM01.** Table 3 displays the comparison results with state-of-the-art VI-ReID methods on the SYSU-MM01 dataset. From the perspective of evaluation settings, *i.e.* *all-search/indoor-search* and *single-shot/multi-shot*, we obtain two observations. First, the results of all the methods under the *indoor-search* setting are better than those under the *all-search* setting. This is because the images in the *indoor-search* setting only contain relatively brief indoor scenarios, while those in the *all-search* setting have more complex in-the-wild scenarios. Second, for a same method, the results under the *multi-shot* setting are better than those under the *single-shot* setting in terms of Rank accuracies, while the phenomenon is opposite in terms of mAP scores. This is due to the fact that each person identity contains 10 gallery images in the *multi-shot* setting and only has 1 gallery image in the *single-shot* setting. As a result, for *multi-shot*, it is easier to match one right sample according to the ranking of similarity scores, but more difficult to match all right samples. The following analyses are based on the *single-shot&all-search* setting, since it is more challenging as mentioned in [42, 14].

Table 3. Comparisons with state-of-the-art methods on the SYSU-MM01 dataset. cm-SSFT\* denotes that we report the results of cm-SSFT under the single-query setting [30] for fair comparisons with other methods. CM-NAS<sup>†</sup> means searching a neural architecture on the RegDB dataset and then training the searched neural network on the SYSU-MM01 dataset with the loss function Eq. (12).

| Method                 | Venue    | All-Search   |              |              |              |              |              |              |             | Indoor-Search |              |              |              |              |              |              |              |
|------------------------|----------|--------------|--------------|--------------|--------------|--------------|--------------|--------------|-------------|---------------|--------------|--------------|--------------|--------------|--------------|--------------|--------------|
|                        |          | Single-Shot  |              |              |              | Multi-Shot   |              |              |             | Single-Shot   |              |              |              | Multi-Shot   |              |              |              |
|                        |          | R1           | R10          | R20          | mAP          | R1           | R10          | R20          | mAP         | R1            | R10          | R20          | mAP          | R1           | R10          | R20          | mAP          |
| Zero-Pad [46]          | ICCV-17  | 14.80        | 54.12        | 71.33        | 15.95        | 19.13        | 61.40        | 78.41        | 10.89       | 20.58         | 68.38        | 85.79        | 26.92        | 24.43        | 75.86        | 91.32        | 18.64        |
| TONE [53]              | AAAI-18  | 12.52        | 50.72        | 68.60        | 14.42        | -            | -            | -            | -           | 20.82         | 68.86        | 84.46        | 26.38        | -            | -            | -            | -            |
| HCML [53]              | AAAI-18  | 14.32        | 53.16        | 69.17        | 16.16        | -            | -            | -            | -           | 24.52         | 73.25        | 86.73        | 30.08        | -            | -            | -            | -            |
| cmGAN [5]              | IJCAI-18 | 26.97        | 67.51        | 80.56        | 27.80        | 31.49        | 72.74        | 85.01        | 22.27       | 31.63         | 77.23        | 89.18        | 42.19        | 37.00        | 80.94        | 92.11        | 32.76        |
| BDTR [54]              | IJCAI-18 | 27.32        | 66.96        | 81.07        | 27.32        | -            | -            | -            | -           | 31.92         | 77.18        | 89.28        | 41.86        | -            | -            | -            | -            |
| eBDTR [54]             | TIFS-19  | 27.82        | 67.34        | 81.34        | 28.42        | -            | -            | -            | -           | 32.46         | 77.42        | 89.62        | 42.46        | -            | -            | -            | -            |
| HSME [14]              | AAAI-19  | 20.68        | 62.74        | 77.95        | 23.12        | -            | -            | -            | -           | -             | -            | -            | -            | -            | -            | -            | -            |
| D <sup>2</sup> RL [45] | CVPR-19  | 28.9         | 70.6         | 82.4         | 29.2         | -            | -            | -            | -           | -             | -            | -            | -            | -            | -            | -            | -            |
| MSR [10]               | TIP-19   | 37.35        | 83.40        | 93.34        | 38.11        | 43.86        | 86.94        | 95.68        | 30.48       | 39.64         | 89.29        | 97.66        | 50.88        | 46.56        | 93.57        | 98.80        | 40.08        |
| AlignGAN [42]          | ICCV-19  | 42.4         | 85.0         | 93.7         | 40.7         | 51.5         | 89.4         | 95.7         | 33.9        | 45.9          | 87.6         | 94.4         | 54.3         | 57.1         | 92.7         | 97.4         | 45.3         |
| JSIA-ReID [43]         | AAAI-20  | 38.1         | 80.7         | 89.9         | 36.9         | 45.1         | 85.7         | 93.8         | 29.5        | 43.8          | 86.2         | 94.2         | 52.9         | 52.7         | 91.1         | 96.4         | 42.7         |
| Xmodal [22]            | AAAI-20  | 49.92        | 89.79        | 95.96        | 50.73        | -            | -            | -            | -           | -             | -            | -            | -            | -            | -            | -            | -            |
| cm-SSFT* [30]          | CVPR-20  | 47.7         | -            | -            | 54.1         | 57.4         | -            | -            | <b>59.1</b> | -             | -            | -            | -            | -            | -            | -            | -            |
| MACE [52]              | TIP-20   | 51.64        | 87.25        | 94.44        | 50.11        | -            | -            | -            | -           | 57.35         | 93.02        | 97.47        | 64.79        | -            | -            | -            | -            |
| DDAG [55]              | ECCV-20  | 54.75        | 90.39        | 95.81        | 53.02        | -            | -            | -            | -           | 61.02         | 94.06        | 98.41        | 67.98        | -            | -            | -            | -            |
| HAT [56]               | TIFS-20  | 55.29        | 92.14        | 97.36        | 53.89        | -            | -            | -            | -           | 62.10         | 95.75        | 99.20        | 69.37        | -            | -            | -            | -            |
| CM-NAS                 | -        | <b>61.99</b> | <b>92.87</b> | <b>97.25</b> | <b>60.02</b> | <b>68.68</b> | <b>94.92</b> | <b>98.36</b> | 53.45       | <b>67.01</b>  | <b>97.02</b> | <b>99.32</b> | <b>72.95</b> | <b>76.48</b> | <b>98.68</b> | <b>99.91</b> | <b>65.11</b> |
| CM-NAS <sup>†</sup>    | -        | 60.42        | 91.86        | 96.76        | 58.62        | 67.87        | 94.49        | 98.11        | 52.07       | 66.74         | 96.14        | 99.27        | 72.37        | 75.69        | 97.93        | 99.76        | 64.27        |

Table 4. Comparisons with state-of-the-art methods on the RegDB dataset. CM-NAS<sup>†</sup> means searching a neural architecture on the SYSU-MM01 dataset and then training the searched neural network on the RegDB dataset with the loss function Eq. (12).

| Method                 | Visible to Infrared |              |              |              | Infrared to Visible |              |              |              |
|------------------------|---------------------|--------------|--------------|--------------|---------------------|--------------|--------------|--------------|
|                        | R1                  | R10          | R20          | mAP          | R1                  | R10          | R20          | mAP          |
| Zero-Pad [46]          | 17.74               | 34.21        | 44.35        | 18.90        | 16.63               | 34.68        | 44.25        | 17.82        |
| HCML [53]              | 24.44               | 47.53        | 56.78        | 20.08        | 21.70               | 45.02        | 55.58        | 22.24        |
| BDTR [54]              | 33.56               | 58.61        | 67.43        | 32.76        | 32.92               | 58.46        | 68.43        | 31.96        |
| eBDTR [54]             | 34.62               | 58.96        | 68.72        | 33.46        | 34.21               | 58.74        | 68.64        | 32.49        |
| HSME [14]              | 50.85               | 73.36        | 81.66        | 47.00        | 50.15               | 72.40        | 81.07        | 46.16        |
| D <sup>2</sup> RL [45] | 43.4                | 66.1         | 76.3         | 44.1         | -                   | -            | -            | -            |
| MAC [52]               | 36.43               | 62.36        | 71.63        | 37.03        | 36.20               | 61.68        | 70.99        | 36.63        |
| MSR [10]               | 48.43               | 70.32        | 79.95        | 48.67        | -                   | -            | -            | -            |
| AlignGAN [42]          | 57.9                | -            | -            | 53.6         | 56.3                | -            | -            | 53.4         |
| JSIA-ReID [43]         | 48.5                | -            | -            | 49.3         | 48.1                | -            | -            | 48.9         |
| Xmodal [22]            | 62.21               | 83.13        | 91.72        | 60.18        | -                   | -            | -            | -            |
| cm-SSFT* [30]          | 65.4                | -            | -            | 65.6         | 63.8                | -            | -            | 64.2         |
| MACE [52]              | 72.37               | 88.40        | 93.59        | 69.09        | 72.12               | 88.07        | 93.07        | 68.57        |
| DDAG [55]              | 69.34               | 86.19        | 91.49        | 63.46        | 68.06               | 85.15        | 90.31        | 61.80        |
| HAT [56]               | 71.83               | 87.16        | 92.16        | 67.56        | 70.02               | 86.45        | 91.61        | 66.30        |
| CM-NAS                 | <b>84.54</b>        | <b>95.18</b> | <b>97.85</b> | <b>80.32</b> | <b>82.57</b>        | <b>94.51</b> | <b>97.37</b> | <b>78.31</b> |
| CM-NAS <sup>†</sup>    | 82.68               | 94.79        | 97.58        | 78.91        | 81.24               | 93.85        | 96.65        | 77.16        |

From the perspective of methods, our CM-NAS outperforms all the competitors by a large margin. For instance, compared with the state-of-the-art HAT, we improve the Rank-1 accuracy and the mAP score by **6.70%** and **6.13%**, respectively. Meanwhile, it is worth noting that the image size of the input of HAT is  $288 \times 144$ , while that of our method is  $256 \times 128$ . The significant improvements with a smaller image size fully demonstrate the superiority of our method. Furthermore, we also conduct a cross-dataset experiment to evaluate the generalization ability of the searched neural architecture. We first search a neural architecture on the RegDB dataset, and then train the searched neural architecture on the SYSU-MM01 dataset with the loss function Eq. (12). Such a cross-dataset method is denoted as CM-NAS<sup>†</sup> in Table 3. It is obvious that CM-NAS<sup>†</sup> still significantly surpasses all the state-of-the-art methods,

revealing the great generalization ability of the searched cross-modality neural architecture.

**Comparisons on RegDB.** As listed in Table 4, we observe that our CM-NAS has significant advantages over other state-of-the-art VI-ReID methods on the RegDB dataset. Under the *Visible to Infrared* setting, CM-NAS exceeds the state-of-the-art MACE by **12.17%** and **11.23%** in terms of the Rank-1 accuracy and the mAP score, respectively. When switching to the *Infrared to Visible* setting, compared with MACE, CM-NAS still improves the Rank-1 accuracy and the mAP score by **10.45%** and **9.74%**, respectively. Besides, we also study the aforementioned cross-dataset method CM-NAS<sup>†</sup>, in which the neural architecture is searched on the SYSU-MM01 dataset and then trained on the RegDB dataset with the loss function Eq. (12). Table 4 shows that CM-NAS<sup>†</sup> is always superior to all the state-of-the-art methods, which further verifies the generalization ability of the searched neural architecture.

## 5. Conclusion

This paper has presented a novel CM-NAS to tackle the challenging VI-ReID. To begin with, we systematically investigate the manually designed neural architectures and find that appropriately splitting BN layers to learn modality-specific representations can yield better performances. It motivates us to develop a BN-oriented NAS algorithm that has the ability to automatically decide the splitting of BN layers, searching the optimal architecture. Subsequently, in order to better guide the search process, we further propose a new C<sup>3</sup>MMD loss. It not only reduces the modality discrepancy, but also maintains the consistency of the similarity correlations that have been overlooked before in the VIS



and the IR modalities. Finally, extensive experimental results on two popular VI-ReID datasets verify the superiority of our method.

## References

- [1] Song Bai, Xiang Bai, and Qi Tian. Scalable person re-identification on supervised smoothed manifold. In *CVPR*, 2017.
- [2] Bowen Baker, Otakrist Gupta, Nikhil Naik, and Ramesh Raskar. Designing neural network architectures using reinforcement learning. In *ICLR*, 2017.
- [3] Han Cai, Ligeng Zhu, and Song Han. Proxylessnas: Direct neural architecture search on target task and hardware. In *ICLR*, 2019.
- [4] Xin Chen, Lingxi Xie, Jun Wu, and Qi Tian. Progressive differentiable architecture search: Bridging the depth gap between search and evaluation. In *ICCV*, 2019.
- [5] Pingyang Dai, Rongrong Ji, Haibin Wang, Qiong Wu, and Yuyu Huang. Cross-modality person re-identification with generative adversarial training. In *IJCAI*, 2018.
- [6] Xiaoliang Dai, Peizhao Zhang, Bichen Wu, Hongxu Yin, Fei Sun, Yanghan Wang, Marat Dukhan, Yunqing Hu, Yiming Wu, Yangqing Jia, Peter Vajda, Matt Uyttendaele, and Niraj K. Jha. Chamnet: Towards efficient network design through platform-aware model adaptation. In *CVPR*, 2019.
- [7] Shengyong Ding, Liang Lin, Guangrun Wang, and Hongyang Chao. Deep feature learning with relative distance comparison for person re-identification. *PR*, 2015.
- [8] Xuanyi Dong and Yi Yang. Searching for a robust neural architecture in four gpu hours. In *CVPR*, 2019.
- [9] Jiemin Fang, Yuzhu Sun, Qian Zhang, Yuan Li, Wenyu Liu, and Xinggang Wang. Densely connected search space for more flexible neural architecture search. In *CVPR*, 2020.
- [10] Zhanxiang Feng, Jianhuang Lai, and Xiaohua Xie. Learning modality-specific representations for visible-infrared person re-identification. *TIP*, 2019.
- [11] Chaoyou Fu, Xiang Wu, Yibo Hu, Huaibo Huang, and Ran He. Dual variational reneration for low shot heterogeneous face recognition. In *NeurIPS*, 2019.
- [12] Shaogang Gong, Marco Cristani, Shuicheng Yan, and Chen Change Loy. Person re-identification. 2016.
- [13] Arthur Gretton, Karsten Borgwardt, Malte Rasch, Bernhard Schölkopf, and Alex J Smola. A kernel method for the two-sample-problem. In *NeurIPS*, 2007.
- [14] Yi Hao, Nannan Wang, Jie Li, and Xinbo Gao. Hsme: Hypersphere manifold embedding for visible thermal person re-identification. In *AAAI*, 2019.
- [15] Kaiming He, Xiangyu Zhang, Shaoqing Ren, and Jian Sun. Deep residual learning for image recognition. In *CVPR*, 2016.
- [16] Lingxiao He, Jian Liang, Haiqing Li, and Zhenan Sun. Deep spatial feature reconstruction for partial person re-identification: Alignment-free approach. In *CVPR*, 2018.
- [17] Alexander Hermans, Lucas Beyer, and Bastian Leibe. In defense of the triplet loss for person re-identification. *arXiv:1703.07737*, 2017.
- [18] Yibo Hu, Xiang Wu, and Ran He. Tf-nas: Rethinking three search freedoms of latency-constrained differentiable neural architecture search. In *ECCV*, 2020.
- [19] Sergey Ioffe and Christian Szegedy. Batch normalization: Accelerating deep network training by reducing internal covariate shift. *arXiv:1502.03167*, 2015.
- [20] Martin Koestinger, Martin Hirzer, Paul Wohlhart, Peter M Roth, and Horst Bischof. Large scale metric learning from equivalence constraints. In *CVPR*, 2012.
- [21] Qingming Leng, Mang Ye, and Qi Tian. A survey of open-world person re-identification. *TCSVT*, 2019.
- [22] Diangang Li, Xing Wei, Xiaopeng Hong, and Yihong Gong. Infrared-visible cross-modal person re-identification with an x modality. In *AAAI*, 2020.
- [23] Wei Li, Xiatian Zhu, and Shaogang Gong. Person re-identification by deep joint learning of multi-loss classification. In *IJCAI*, 2017.
- [24] Wei Li, Xiatian Zhu, and Shaogang Gong. Harmonious attention network for person re-identification. In *CVPR*, 2018.
- [25] Shengcai Liao, Yang Hu, Xiangyu Zhu, and Stan Z Li. Person re-identification by local maximal occurrence representation and metric learning. In *CVPR*, 2015.
- [26] Shengcai Liao and Stan Z Li. Efficient psd constrained asymmetric metric learning for person re-identification. In *ICCV*, 2015.
- [27] Haijun Liu, Jian Cheng, Wen Wang, Yanzhou Su, and Haiwei Bai. Enhancing the discriminative feature learning for visible-thermal cross-modality person re-identification. *Neurocomputing*, 2020.
- [28] Hanxiao Liu, Karen Simonyan, and Yiming Yang. Darts: Differentiable architecture search. In *ICLR*, 2019.
- [29] Mingsheng Long, Jianmin Wang, Guiguang Ding, Jianguang Sun, and Philip S Yu. Transfer feature learning with joint distribution adaptation. In *ICCV*, 2013.
- [30] Yan Lu, Yue Wu, Bin Liu, Tianzhu Zhang, Baopu Li, Qi Chu, and Nenghai Yu. Cross-modality person re-identification with shared-specific feature transfer. In *CVPR*, 2020.
- [31] Hao Luo, Youzhi Gu, Xingyu Liao, Shenqi Lai, and Wei Jiang. Bag of tricks and a strong baseline for deep person re-identification. In *CVPR Workshops*, 2019.
- [32] Bingpeng Ma, Yu Su, and Frederic Jurie. Covariance descriptor based on bio-inspired features for person re-identification and face verification. *IVC*, 2014.
- [33] Dat Tien Nguyen, Hyung Gil Hong, Ki Wan Kim, and Kang Ryoung Park. Person recognition system based on a combination of body images from visible light and thermal cameras. *Sensors*, 2017.
- [34] Sinno Jialin Pan, Ivor W Tsang, James T Kwok, and Qiang Yang. Domain adaptation via transfer component analysis. *TNNLS*, 2010.
- [35] Baoyun Peng, Xiao Jin, Jiaheng Liu, Dongsheng Li, Yichao Wu, Yu Liu, Shunfeng Zhou, and Zhaoning Zhang. Correlation congruence for knowledge distillation. In *ICCV*, 2019.
- [36] Esteban Real, Alok Aggarwal, Yanping Huang, and Quoc V Le. Regularized evolution for image classifier architecture search. In *AAAI*, 2019.

- [37] Yifan Sun, Liang Zheng, Yi Yang, Qi Tian, and Shengjin Wang. Beyond part models: Person retrieval with refined part pooling (and a strong convolutional baseline). In *ECCV*, 2018.
- [38] Mingxing Tan, Bo Chen, Ruoming Pang, Vijay Vasudevan, Mark Sandler, Andrew Howard, and Quoc V Le. Mnasnet: Platform-aware neural architecture search for mobile. In *CVPR*, 2019.
- [39] Mingxing Tan and Quoc V Le. Efficientnet: Rethinking model scaling for convolutional neural networks. In *ICML*, 2019.
- [40] Frederick Tung and Greg Mori. Similarity-preserving knowledge distillation. In *ICCV*, 2019.
- [41] Cheng Wang, Qian Zhang, Chang Huang, Wenyu Liu, and Xinggang Wang. Mancs: A multi-task attentional network with curriculum sampling for person re-identification. In *ECCV*, 2018.
- [42] Guan-An Wang, Tianzhu Zhang, Jian Cheng, Si Liu, Yang Yang, and Zengguang Hou. Rgb-infrared cross-modality person re-identification via joint pixel and feature alignment. In *ICCV*, 2019.
- [43] Guan-An Wang, Tianzhu Zhang, Yang Yang, Jian Cheng, Jianlong Chang, Xu Liang, and Zengguang Hou. Cross-modality paired-images generation for rgb-infrared person re-identification. In *AAAI*, 2020.
- [44] Jingya Wang, Xiatian Zhu, Shaogang Gong, and Wei Li. Transferable joint attribute-identity deep learning for unsupervised person re-identification. In *CVPR*, 2018.
- [45] Zhixiang Wang, Zheng Wang, Yinqiang Zheng, Yung-Yu Chuang, and Shin'ichi Satoh. Learning to reduce dual-level discrepancy for infrared-visible person re-identification. In *CVPR*, 2019.
- [46] Ancong Wu, Wei-Shi Zheng, Hong-Xing Yu, Shaogang Gong, and Jianhuang Lai. Rgb-infrared cross-modality person re-identification. In *ICCV*, 2017.
- [47] Bichen Wu, Xiaoliang Dai, Peizhao Zhang, Yanghan Wang, Fei Sun, Yiming Wu, Yuandong Tian, Peter Vajda, Yangqing Jia, and Kurt Keutzer. Fbnet: Hardware-aware efficient convnet design via differentiable neural architecture search. In *CVPR*, 2019.
- [48] Cihang Xie, Mingxing Tan, Boqing Gong, Jiang Wang, Alan L Yuille, and Quoc V Le. Adversarial examples improve image recognition. In *CVPR*, 2020.
- [49] Yuhui Xu, Lingxi Xie, Xiaopeng Zhang, Xin Chen, Guo-Jun Qi, Qi Tian, and Hongkai Xiong. Pc-darts: Partial channel connections for memory-efficient differentiable architecture search. In *ICLR*, 2020.
- [50] Hongliang Yan, Yukang Ding, Peihua Li, Qilong Wang, Yong Xu, and Wangmeng Zuo. Mind the class weight bias: Weighted maximum mean discrepancy for unsupervised domain adaptation. In *CVPR*, 2017.
- [51] Yang Yang, Jimei Yang, Junjie Yan, Shengcai Liao, Dong Yi, and Stan Z Li. Salient color names for person re-identification. In *ECCV*, 2014.
- [52] Mang Ye, Xiangyuan Lan, Qingming Leng, and Jianbing Shen. Cross-modality person re-identification via modality-aware collaborative ensemble learning. *TIP*, 2020.
- [53] Mang Ye, Xiangyuan Lan, Jiawei Li, and Pong C Yuen. Hierarchical discriminative learning for visible thermal person re-identification. In *AAAI*, 2018.
- [54] Mang Ye, Xiangyuan Lan, Zheng Wang, and Pong C Yuen. Bi-directional center-constrained top-ranking for visible thermal person re-identification. *TIFS*, 2019.
- [55] Mang Ye, Jianbing Shen, David J Crandall, Ling Shao, and Jiebo Luo. Dynamic dual-attentive aggregation learning for visible-infrared person re-identification. In *ECCV*, 2020.
- [56] Mang Ye, Jianbing Shen, and Ling Shao. Visible-infrared person re-identification via homogeneous augmented tri-modal learning. *TIFS*, 2020.
- [57] Mang Ye, Zheng Wang, Xiangyuan Lan, and Pong C Yuen. Visible thermal person re-identification via dual-constrained top-ranking. In *IJCAI*, 2018.
- [58] Mang Ye and Pong C Yuen. Purifynet: A robust person re-identification model with noisy labels. *TIFS*, 2020.
- [59] Hong-Xing Yu, Ancong Wu, and Wei-Shi Zheng. Unsupervised person re-identification by deep asymmetric metric embedding. *TPAMI*, 2018.
- [60] Yunpeng Zhai, Shijian Lu, Qixiang Ye, Xuebo Shan, Jie Chen, Rongrong Ji, and Yonghong Tian. Ad-cluster: Augmented discriminative clustering for domain adaptive person re-identification. In *CVPR*, 2020.
- [61] Shizhen Zhao, Changxin Gao, Jun Zhang, Hao Cheng, Chuchu Han, Xinyang Jiang, Xiaowei Guo, Wei-Shi Zheng, Nong Sang, and Xing Sun. Do not disturb me: Person re-identification under the interference of other pedestrians. In *ECCV*, 2020.
- [62] Liang Zheng, Zhi Bie, Yifan Sun, Jingdong Wang, Chi Su, Shengjin Wang, and Qi Tian. Mars: A video benchmark for large-scale person re-identification. In *ECCV*, 2016.
- [63] Liang Zheng, Liye Shen, Lu Tian, Shengjin Wang, Jingdong Wang, and Qi Tian. Scalable person re-identification: A benchmark. In *ICCV*, 2015.
- [64] Liang Zheng, Yi Yang, and Alexander G Hauptmann. Person re-identification: Past, present and future. *arXiv:1610.02984*, 2016.
- [65] Wei-Shi Zheng, Shaogang Gong, and Tao Xiang. Reidentification by relative distance comparison. *TPAMI*, 2012.
- [66] Zhedong Zheng, Xiaodong Yang, Zhiding Yu, Liang Zheng, Yi Yang, and Jan Kautz. Joint discriminative and generative learning for person re-identification. In *CVPR*, 2019.
- [67] Zhedong Zheng, Liang Zheng, and Yi Yang. Unlabeled samples generated by gan improve the person re-identification baseline in vitro. In *ICCV*, 2017.
- [68] Barret Zoph, Vijay Vasudevan, Jonathon Shlens, and Quoc V Le. Learning transferable architectures for scalable image recognition. In *CVPR*, 2018.